Article type: Communication

Emergent Low-Symmetry Phases with Large Property Enhancement in Ferroelectric $KNbO_3$ Bulk Crystals

*Tom T. A. Lummen, J. Leung, Amit Kumar, X. Wu, Y. Ren, Brian K. Vanleeuwen, Ryan C. Haislmaier, Martin Holt, Keji Lai, Sergei V. Kalinin, Venkatraman Gopalan**

T. T. A. Lummen, J. Leung, B. K. VanLeeuwen, R. C. Haislmaier, and V. Gopalan

Department of Materials Science and Engineering, Pennsylvania State University, University Park, Pennsylvania 16802, USA

Email: vgopalan@psu.edu

A. Kumar

School of Mathematics and Physics, Queen's University Belfast, University Road, Belfast, BT71NN, Northern Ireland, UK

S. Kalinin

Center for Nanophase Materials Sciences, Oak Ridge National Laboratory, Oak Ridge, Tennessee 37831, USA

X. Wu, Y. Ren, and K. Lai

Department of Physics, University of Texas at Austin, Austin, Texas ZIP, USA

M. Holt

Center for Nanoscale Materials, Argonne National Laboratory, Argonne, Illinois 60439, USA

Keywords: ferroelectrics, thermotropic phase boundary, low-symmetry phase, conducting domain walls

Abstract

In search of enhanced ferroelectric and optical properties in materials, one traditionally searches the chemical composition space. Such property enhancements may however also be hidden within already well-known materials when their structural symmetry is lowered from their equilibrium state through a small local strain. Using optical second harmonic generation microscopy, piezoelectric force microscopy, microwave imaging microscopy and hard X-ray diffraction microscopy of bulk crystals of $KNbO_3$, a new metastable phase with monoclinic symmetry was found. The phase, which co-exists with the orthorhombic phase at room temperature, is induced by local strains generated by a network of ferroelectric domain walls. While the local microstructural shear strain involved is small, on the order of ~0.017% with respect to the pseudocubic reference cell, the concurrent symmetry reduction results in an optical second harmonic generation response that is over 550% higher (an increase in the effective nonlinear coefficients of ~234%) at room temperature. Consistent with the picture of the domain microstructure inducing out-of-equilibrium material properties, the meandering walls of the low symmetry domains also exhibit enhanced electrical conductivity on the order of 1 S m^{-1}.. Thus, symmetry lowering through domain microstructure engineering may be a viable route to designing large property enhancements and conductivity tuning in bulk ferroelectric crystals.

Metastable intermediate states in materials can lead to large property enhancements if stabilized by composition, pressure, bulk strain, or fields. Prominent examples of such functional property enhancements can be found in the lead-based solid solution perovskites that exhibit large piezoelectric coefficients near a morphotropic phase boundary (MPB) [1-4] or colossal magnetoresistance near a magnetic transition. Considerable scientific effort has been devoted to find more benign (i.e lead-free) high-performance piezoelectrics, which would offer comparable performance.[5-14] In thin films, biaxial strain tuning with 1-6% strains has been demonstrated to be powerful for inducing emergent phenomena and property enhancements.[15-17] In bulk single crystals this is a challenge since practical strains are on the order of 0.01-0.1%.[18] Recently, Lummen *et al*. showed that even in single crystals of simple ferroelectrics such as $BaTiO_3$, such symmetry lowering and property enhancements can be achieved through a network of domain walls that create local shear strains of ~0.01% and fields of ~10^6V/m.[19] As a thermal analogue of an MPB, such a phase boundary has been termed a thermotropic phase boundary (TPB). Here we present an experimental study of a domain engineered $KNbO_3$ single crystal at room temperature, near its rhombohedral-to-orthorhombic thermal phase transition. Despite the different equilibrium phase and very different types of domain walls in the KNO_3 system, we observe new low symmetry phases very similar to those found in thermotropic $BaTiO_3$. The observed phases exhibit significantly enhanced nonlinear optical properties, markedly distinct piezoelectric properties and enhanced domain wall conductivity, thus both generalizing the notion of TPBs in simple ferroelectrics and expanding their possible merits.

$KNbO_3$ exhibits a sequence of phase transitions from rhombohedral (R) to orthorhombic (O) (at ~263K), to tetragonal (T, at ~498K), to cubic (C at ~710K), where the first three are ferroelectric.[20] In the orthorhombic phase (point group *mm2*) at room temperature, the ferroelectric polarization is nominally constrained to one of the symmetry-equivalent face-

diagonals of the perovskite pseudocube,[21, 22] yielding a total of 12 possible orientations of the ferroelectric domains.

To study thermotropic effects in $KNbO_3$ we employ nonlinear optical second harmonic generation (SHG), which is highly sensitive to the presence, symmetry and property enhancement of polar phases.[19, 23] **Figure 1a** shows a scanning SHG microscopy map of a large area of a $KNbO_3$ single crystal after thermal cycling, revealing a complex and densely twinned domain structure. From the crystal geometry (X, Y and Z are parallel to the pseudocubic (pc) perovskite axes, see **Figure 1b**) and the nominal domain wall orientations in orthorhombic perovskites,[24] one can deduce that the majority of the observed domains are oriented such that the ferroelectric polarization lies in the XZ plane, along one of four the symmetry-equivalent $<101>_{pc}$ axes.[21, 22] For the sake of argument, we define the orthorhombic domains labeled $O_{XZ,1}$ to have their ferroelectric polarization $\mathbf{P}_S$ along the $[101]_{pc}$ direction in the XYZ reference frame.[25] As can be seen in the SHG image, the $O_{XZ,1}$ domains are neighbored by $O_{XZ,2}$ domains (both of low relative SHG intensity), separated by 90° domain walls oriented parallel to the $(100)_{pc}$ plane (vertical dashed arrows in Figure 1a). This creates a domain matrix of ferroelectric polarization in the XZ plane, in which the Z-component of the polarization alternates between domains. Throughout this domain matrix, both the $O_{XZ,1}$ and $O_{XZ,2}$ domains are interspersed with thin 'sliver' (needle-like) domains (very low relative SHG intensity), with the surface projections of the corresponding domains walls parallel to the $[110]_{pc}$ and $[1\text{-}10]_{pc}$ directions. These orthorhombic sliver domains have a ferroelectric polarization in the YZ plane, nominally forming 120° domain walls with their neighboring O_{XZ} domains.

Within the orthorhombic domain matrix in Figure 1a**,** we observe large regions of strongly enhanced SHG intensity (labeled *M*), characterized by meandering borders and intensity ripples. In addition, one observes several of these regions being delineated by the 90° domains walls (parallel to the (100) plane) of the underlying orthorhombic domain matrix.

Reminiscent of thermotropic $BaTiO_3$, these regions are associated to low symmetry phases, which we next probe using spatially resolved SHG polarimetry (see Supplementary Information for details). As shown in **Figure 1c**, the theoretical SHG response for an orthorhombic *mm2* domain (solid lines, **Equation S5**, Supplementary Information) yields an excellent fit to the experimental polarimetry data (data points). This dataset was measured in the orthorhombic domain matrix (position 1), and thus confirms both the symmetry and polarization plane of the O_{XZ} domains. For the *M* domains of the new phase, we anticipate a local symmetry lowering corresponding to a rotation of the ferroelectric polarization, such that only one of the two orthorhombic mirror planes survives. The resulting monoclinic model (point group *m*, **Equation S8**, Supplementary Information) fits the experimental data very well (see **Figure 1d)**. To quantify the SHG intensity enhancements in the *M* phase, **Figure 1e** shows the $I^{2\omega}(\theta, 0°)$ polarimetry data of a series of points (taken under the same experimental conditions on positions 2 through 6, see Figure 1a) for direct comparison. Compared to that in the O_{XZ} reference domain (point 2), the SHG intensity measured at points 3 through 6 is enhanced by 180, 640, 276 and 558%, respectively. These enhancements are attributed to the altered and newly active d_{ij}^{m} coefficients in the lower symmetry *M* phase (see Equation S8). The spatial variation of the SHG intensity within the *M* domains is likely related to a corresponding variation of the degree and sign of the underlying structural distortion.[19]

One notable feature of these *M* domains is the fact that in many cases they are rather abruptly delimited by 90° domains walls in the surrounding O_{XZ} domain matrix (see Figure 1a). We propose the following underlying mechanism: within the domain structure of Figure 1a, one can observe several O_{YZ} sliver domains that continue across the 90° O_{XZ} domain walls (see for example, the region indicated by the white rectangle). As sketched in **Figure 1f**, if such a sliver domain is embedded in both O_{XZ} domains, its domain wall type necessarily changes across the O_{XZ}-O_{XZ} boundary from a 120° domain wall on one side to a 60° domain wall on the other. Moreover, since the domain wall orientation is the same on both sides of the boundary (parallel

to the (-110) plane in the example of Figure 1f), the 60° domain wall is forced to adopt a crystallographic wall orientation that is both mechanically incompatible and charged,[24, 26] inducing localized internal stresses and electric fields only on that side of the O_{XZ}-O_{XZ} boundary (the right side in the example of Figure 1f). As a result, the corresponding structural distortions, symmetry lowering and altered properties are delimited by that boundary.

Next we employ piezoresponse force microscopy (PFM) to probe the local piezoresponse in the $KNbO_3$ domain microstructure. **Figure 2** shows a direct comparison between a scanning SHG microscopy map ($I^{2\omega}(\theta, 0°)$, panel a) and scanning PFM images (panels b and c) recorded in the same area of the highly twinned domain structure. As in Figure 1, the SHG map reveals an O_{XZ} domain matrix interspersed with O_{YZ} sliver domains, contrasted by a large *M* domain of strongly enhanced SHG intensity. The *M* domain exhibits characteristic SHG intensity ripples and is delineated on the left by a 90° orthorhombic domain wall, and on the right by a domain wall that meanders along a wide range of orientations, rather than following symmetry-prescribed crystallographic planes.[24] This is a further indication of local symmetry lowering. The corresponding lateral PFM maps (**Figure 2b and 2c**), which nominally probe the d_{32} piezoelectric coefficient of the O_{XZ} domains in the current configuration, exhibit a strikingly similar contrast of the *M* domain, showing that its in-plane piezoresponse is enhanced with respect to that of orthorhombic $KNbO_3$. Maps of the corresponding out-of-plane PFM signal (vertical PFM, see **Figure S1**), which nominally contains a combination of d_{31}, d_{33}, and d_{15} piezoelectric coefficients, also show a clearly distinct piezoresponse in the *M* domain. In contrast to the PFM maps, the SHG signal consistently exhibits Moiré-like intensity ripples within the *M* domains. This difference is tentatively ascribed to monoclinic twinning (i.e. a spatial distribution of the magnitude and direction of the symmetry-lowering structural distortion), as was observed for $BaTiO_3$. We surmise that this would predominantly affect the

phase of local responses, which could lead to interference effects within the relatively large SHG probing volume while being undetected in PFM due to the smaller probe size.

In light of the recent reports on conductive ferroelectric DWs,[27] we performed scanning microwave impedance microscopy (MIM)[28, 29] in order to clarify the electrical properties of various DWs in this sample. The MIM measures the complex tip-sample admittance at 1 GHz, from which the local permittivity and conductivity can be extracted.[30] **Figure 2d** shows the PFM map of a similar sample area, again composed of an O_{XZ} domain matrix interspersed with O_{YZ} sliver domains, contrasted by a large M domain exhibiting a clearly distinct piezoresponse and meandering domain walls (DWs). **Figure 2e and 2f** show the real (MIM-Re) and imaginary (MIM-Im) parts of the MIM map in the same area, respectively. The meandering borders of the *M* domain are clearly seen in the MIM-Re image but indiscernible in the MIM-Im data. Note that the apparent width of the conductive borders is limited by the spatial resolution of the MIM (comparable to the tip diameter of ~200 nm in this experiment), rather than the actual DW width. Since both the *M* and different orthorhombic domains are highly insulating, we can estimate the local conductivity of the *M*-O_{XZ} DWs to be on the order of 1 S m^{-1}, a typical value for conductive DWs in other ferroelectrics such as $BiFeO_3$[31] and PZT,[32] by using finite-element analysis (FEA).[30] Details of the FEA simulation are included in the Supporting Information. We further note the absence of such conductivity enhancements along the walls between the O_{YZ} sliver domains and the O_{XZ} domain matrix. Following recent reports of enhanced conductivity in both magnetic DWs in a magnetic insulator[33] and charge-ordered DWs in a layered manganite,[34] these results suggest the existence of similar conductive wall properties in the microstructure-induced low-symmetry phases in thermotropic ferroelectrics.

Given the previously established close relation between symmetry, properties and crystal structure in TPB materials,[19] $KNbO_3$ was also studied using scanning X-ray Diffraction Microscopy (SXDM).[35, 36] SXDM employs a focused, highly monochromatic x-ray beam to locally probe the microscopic structure of the sample, as sketched in **Figure 3a**. Typically, when

the incident angular spread is centered on that particular diffraction condition, the corresponding detected diffraction peak appears as two vertically separated lobes, whose angular center of mass (COM) reflects the associated ($2\theta,\chi$) coordinate (see example in **Figure 3a**). Here the SXDM experiments centered on the (202) diffraction peak of the $O_{XZ,1}$ matrix domains, which corresponds to the set of pseudocubic planes parallel to the sample surface (see **Figure 3b**). **Figure 3c** plots the resulting $(202)_O$ diffraction recorded from four selected locations on the $KNbO_3$ sample. In each case, several well-defined diffraction peaks are observed simultaneously, corresponding to different domains situated at different depths, which are simultaneously probed due to the diagonally elongated probing volume and the resulting angular depth-probing effect (see Experimental Section). Despite the complexity of the probing geometry, the SXDM results can be qualitatively interpreted by analyzing the angular center-of-mass of the integrated intensity of the diffraction multiplets.[19] **Figure 3d** shows an SXDM image of the highly twinned area of the $KNbO_3$ sample, corresponding to a spatial map of the 2θ-center-of-mass (COM) of the diffraction peak multiplet. **Figure 3e** shows the corresponding scanning SHG image recorded in the same area. As can be seen from the latter, this area is also composed of an O_{XZ} domain matrix interspersed with O_{YZ} domains, with a large *M* domain delineated by the rightmost orthorhombic 90° domain wall. As is evident from the representative diffraction signals shown in **Figure 3c**, and from comparison with the SXDM image, the 2θ-center-of-mass of the diffraction multiplets throughout the *M* domain is significantly upshifted with respect to that of the $O_{XZ,1}$ domain, indicating a significant structural change. The results are qualitatively consistent with an overall deformation in the *M* domain caused by a simple shear distortion of the structural pseudocubic matrix in the XZ plane (see **Figure 3f**). This distortion correspondingly reduces the local point group symmetry to *m*, with the surviving mirror plane parallel to the XZ plane, which is in excellent agreement with the symmetry conclusions resulting from the SHG polarimetry. By assuming the average relative 2θ-shift of the *M* domain ($\langle \Delta 2\theta_M - \Delta 2\theta_O \rangle$ ~0.37 mrad = 0.021°) to be entirely due to

shearing of the pseudocubic matrix, one can roughly estimate the shearing angle δ_M as $\Delta 2\theta_{av.}/2$ ~0.01° (a shear strain of ~0.017%), which is the same order of magnitude as was found for the shear distortion of the monoclinic phase in thermotropic $BaTiO_3$.[19]

Concluding, we find that nominally orthorhombic $KNbO_3$ exhibits the hallmark features of thermotropic behavior at room temperature: local shear strains of only ~0.017% leading to reduced crystallographic symmetry from an *mm*2 to an *m* point group, a corresponding large increase in nonlinear the effective nonlinear coefficients (~234%), and newly active piezoelectric coefficients leading to a distinct piezoresponse. Moreover, the meandering boundaries of the low-symmetry domains exhibit enhanced conductivity on the order of 1 S m^{-1}, providing further evidence for the intertwined roles of local stresses, fields and charges in domain-engineered thermotropic ferroelectrics.

Experimental Section

Sample Preparation: A $KNbO_3$ single crystal was purchased from Oxide Corporation, Japan, cut with surfaces cut parallel to pseudocubic $(100)_{pc}$ planes (pc label = pseudocubic), and resulting crystal surfaces were polished to obtain satisfactory optical surface quality. Prior to experimental investigation, the samples were first annealed at 1100 K for 6h, under a continuous 70 cm^3 min^{-1} O_2 flow, before being cooled to 150 K in a liquid nitrogen-cooled cryostat and kept at that temperature for 1h. Next, the samples were allowed to slowly re-equilibrate to ambient temperature (295 K), resulting in a typical multi-domain structure featuring densely twinned orthorhombic domains. To allow for direct comparison, after thermal cycling the samples were kept at ambient temperature (295 K) in between and during all experiments described in this work.

Optical Second Harmonic Generation (SHG): Optical SHG microscopy and polarimetry were performed in reflection geometry using a customized Witec Alpha 300S confocal Raman microscope equipped with a 10 nm-resolution XYZ piezo-translation stage. The technique,

system and methodology are discussed in detail in Denev *et al.*[23] The pseudocubic axes of the sample were carefully oriented along the X and Y axes of the experimental coordinate system. A 80 MHz train of 800 nm, 100 fs pulses, generated by a Spectra-Physics Tsunami (Ti:Sapphire) and optically chopped at 730 Hz, was focused on the sample using a ×100 or ×40 microscope objective (Nikon, N.A. 0.9 or 0.6, respectively) at a typical incident power density of ~100 pJ mm^{-2} $pulse^{-1}$. The lateral spatial resolution was close to diffraction-limited at the corresponding N.A value (roughly half the fundamental wavelength). A zero-order half-wave plate mounted in a motorized rotational stage controlled the polarization of the fundamental pulse train. The second harmonic (2ω) signal was collected using the same objective, spectrally filtered and passed through a polarization analyzer prior to detection using a Hamamatsu R928 photomultiplier tube. Nonlinear optical $\boldsymbol{d_{ijk}}$ coefficients were calculated using reference values for orthorhombic $KNbO_3$ taken from literature,[37-39] and were scaled using Miller's Δ where needed.[19, 40, 41] All SHG experiments described in this work were performed in air, at ambient pressure and temperature (1 atm, 295 K). Monoclinic SHG signatures were monitored as a function of time after thermal cycling and found to be stable up to at least 14 months when samples were kept at 295 ± 2 K.

Piezoresponse Force Microscopy (PFM): Single-frequency PFM was performed on a Cypher AFM (Asylum Research) using Cr/Pt coated conductive tips (Multi-75E-G, Budget Sensors / PPP-EFM-50, Nanosensors) at the Center for Nanophase Materials Sciences (CNMS) at Oak Ridge National Laboratory, and on a customized AFM system (ParkAFM XE-70) using conductive probes (Multi-75E-G, Budget Sensors) at UT Austin. Typical PFM imaging scan sizes were 30×30 μm, divided into a grid of 256×256 points. Varying AC driving voltages of in the range from 1 to 5 V were used, with driving frequencies of 285 kHz (vertical PFM) and 654 kHz (lateral PFM) in the CNMS setup (tuned 5 kHz below resonance in each case), and 7 kHz in the UT Austin setups, respectively. All PFM measurements were performed under ambient conditions (1 atm, 295).

Microwave impedance microscopy (MIM): MIM scans were conducted on the AFM platform (ParkAFM XE-70) under ambient conditions (1 atm, 295 K) at UT Austin. Commercially available shielded cantilever probes from PrimeNano Inc.[29] were used in the experiment. Details of the MIM technique and setup can be found in Lai *et al*.[28] Before each measurement, the MIM was calibrated using a standard sample (patterned Al dots on SiO_2) such that the two orthogonal channels were proportional to the real (resistive) and imaginary (capacitive) parts of the complex probe-sample microwave admittance. A microwave source frequency of ~1 GHz was employed, at driving amplitudes ranging from 10-100 mV. The typical data acquisition time was 10 ms per pixel for a 256×256 image.

Scanning X-ray Diffraction Microscopy (SXDM):[36] SXDM experiments were performed using the Hard X-ray Nanoprobe (HXN) of the Center for Nanoscale Materials (CNM) at sector 26-ID-C of the Advanced Photon Source, Argonne National Laboratory. The coherent and monochromatic incident X-ray beam (photon energy 9.75 keV, wavelength 0.127 nm) was focused on the sample by a Fresnel zone plate (Xradia Inc., 133 mm diameter gold pattern with 24 nm outer ring width, 1385 rings, and a 300 nm thickness) equipped with a 40 mm diameter centre stop. This yielded a ~30 nm full-width half-maximum (FWHM) lateral beam cross-section in the focal plane. The corresponding focused cone of X-rays had an incident angle spread of ~0.32°. The angle of incidence (~18.3°), photon energy (9.75 keV), and $KNbO_3$ density (4.64 g cm^{-3}) resulted in a ~34 μm x-ray attenuation length, yielding a diagonally elongated SXDM probing volume at an angle to the sample surface, illuminating any domains in this volume and within ~11 μm of the sample surface. The chosen angle of incidence oriented the $KNbO_3$ such that diffraction from the $(202)_O$ planes (O referring to the orthorhombic crystal physics axes) of the most abundant domains (the O_{XZ} domain matrix) was detected using a 2D area CCD detector (Princeton PIXIS-XF: 1024F, 1024×1024 pixels, 13 mm^2 pixel size). Geometrical calibration parameters (sample-detector distance, detector centering and orientation) were determined from diffraction off a purely orthorhombic domain

using the focused beam. CCD images were recorded with 1.6 s of exposure and background-corrected using corresponding 1.6 s dark count images. Imaging of the sample was performed in point-by-point fashion, by scanning the X-ray zone plate relative to the sample using a hybrid optomechanical nanopositioning system. Simultaneous detection of element-specific X-ray fluorescence allowed for positioning with respect to thin silver marker pads, which were patterned on the sample as for positional reference. In order to prevent *in situ* domain structure rearrangement due to surface charging effects, a thin 5 nm layer of gold was deposited on the $KNbO_3$ crystal surfaces and short-circuited to the sample mount. Neither the addition of the silver markers, nor that of the thin short-circuiting layer had a detectable effect on the observed ferroelectric domain structure of the sample, as confirmed by SHG imaging. The relative 2θ-center-of-mass of the diffraction multiplets at each spatial position was calculated according to the method described the Supplementary Information of Lummen *et al*.[19]

Supporting Information

Supporting Information is available from the Wiley Online Library or from the author.

Acknowledgements

T.T.A.L, J.L, B.K.V, R.C.H, and V.G acknowledge support from the National Science Foundation grant numbers DMR-1420620 and DMR-1210588. The BE-PFM measurements in Fig. 5 were performed at the Center for Nanophase Materials Sciences, which is sponsored at Oak Ridge National Laboratory by the Scientific User FacilitiesDivision, Office of Basic Energy Sciences, US Department of Energy. The MIM work (X.W., Y.R., and K.L.) was supported by NSF grant DMR-1649490. Use of the Advanced Photon Source was supported by the U. S. Department of Energy, Office of Science, Office of Basic Energy Sciences, under

Contract No. DE-AC02-06CD11357. V. Gopalan would like to thank beamline ID-26-C at the Advanced Photon Source for providing the Hard X-ray Nanoprobe facilities for the SXDM experiments.

References

[1] B. Noheda, J. A. Gonzalo, L. E. Cross, R. Guo, S. E. Park, D. E. Cox, G. Shirane, Physical Review B 2000, 61, 8687.
[2] B. Noheda, D. E. Cox, G. Shirane, R. Guo, B. Jones, L. E. Cross, Physical Review B 2000, 63, 014103.
[3] R. Guo, L. E. Cross, S. E. Park, B. Noheda, D. E. Cox, G. Shirane, Physical Review Letters 2000, 84, 5423.
[4] B. Noheda, D. E. Cox, Phase Transitions 2006, 79, 5.
[5] D. H. Cho, M. K. Ryu, S. S. Park, S. Y. Cho, J. G. Choi, M. S. Jang, J. P. Kim, C. R. Cho, Journal of the Korean Physical Society 2005, 46, 151.
[6] R. Ahluwalia, T. Lookman, A. Saxena, W. Cao, Physical Review B 2005, 72, 014112.
[7] S. Wada, K. Yako, H. Kakemoto, T. Tsurumi, T. Kiguchi, Journal of Applied Physics 2005, 98, 014109.
[8] S. Wada, T. Muraishi, K. Yokoh, K. Yako, H. Kamemoto, T. Tsurumi, Ferroelectrics 2007, 355, 37.
[9] M. Ahart, M. Somayazulu, R. E. Cohen, P. Ganesh, P. Dera, H.-k. Mao, R. J. Hemley, Y. Ren, P. Liermann, Z. Wu, Nature 2008, 451, 545.
[10] S.-T. Zhang, A. B. Kounga, E. Aulbach, T. Granzow, W. Jo, H.-J. Kleebe, J. Rödel, Journal of Applied Physics 2008, 103, 034107.
[11] S.-E. Park, S. Wada, L. E. Cross, T. R. Shrout, Journal of Applied Physics 1999, 86, 2746.
[12] Y. Xiang, R. Zhang, W. Cao, Journal of Applied Physics 2009, 106, 064102.
[13] T. Sluka, A. K. Tagantsev, D. Damjanovic, M. Gureev, N. Setter, Nature Communications 2012, 3, 748.
[14] C. Ma, H. Guo, S. P. Beckman, X. Tan, Physical Review Letters 2012, 109, 107602.
[15] K. J. Choi, M. Biegalski, Y. L. Li, A. Sharan, J. Schubert, R. Uecker, P. Reiche, Y. B. Chen, X. Q. Pan, V. Gopalan, L. Q. Chen, D. G. Schlom, C. B. Eom, Science 2004, 306, 1005.
[16] O. Diéguez, S. Tinte, A. Antons, C. Bungaro, J. B. Neaton, K. M. Rabe, D. Vanderbilt, Physical Review B 2004, 69, 212101.
[17] D. G. Schlom, L.-Q. Chen, C. J. Fennie, V. Gopalan, D. A. Muller, X. Pan, R. Ramesh, R. Uecker, MRS Bulletin 2014, 39, 118.
[18] S.-E. Park, T. R. Shrout, Journal of Applied Physics 1997, 82, 1804.
[19] T. T. A. Lummen, Y. Gu, J. Wang, S. Lei, F. Xue, A. Kumar, A. T. Barnes, E. Barnes, S. Denev, A. Belianinov, M. Holt, A. N. Morozovska, S. V. Kalinin, L.-Q. Chen, V. Gopalan, Nature Communications 2014, 5, 3172.
[20] G. Shirane, H. Danner, A. Pavlovic, R. Pepinsky, Physical Review 1954, 93, 672.
[21] E. Wiesendanger, Czechoslovak Journal of Physics B 1973, 23, 91.
[22] R. E. Newnham, *Properties of Materials*, Oxford University Press Inc., New York 2005.
[23] S. A. Denev, T. T. A. Lummen, E. Barnes, A. Kumar, V. Gopalan, Journal of the American Ceramic Society 2011, 94, 2699.

[24] P. Marton, I. Rychetsky, J. Hlinka, Physical Review B 2010, 81, 144125.
[25] Note that in the current geometry, it is not possible to distinguish between the four <101> polarization orientations, such that the domain structure proposed here is one of several symmetry-equivalent possibilities.
[26] Y. Gu, F. Xue, S. Lei, T. T. A. Lummen, J. Wang, V. Gopalan, L.-Q. Chen, Physical Review B 2014, 90, 024104.
[27] R. K. Vasudevan, W. Wu, J. R. Guest, A. P. Baddorf, A. N. Morozovska, E. A. Eliseev, N. Balke, V. Nagarajan, P. Maksymovych, S. V. Kalinin, Advanced Functional Materials 2013, 23, 2592.
[28] K. Lai, W. Kundhikanjana, M. A. Kelly, Z.-X. Shen, Applied Nanoscience 2011, 1, 13.
[29] Y. Yongliang, L. Keji, T. Qiaochu, K. Worasom, A. K. Michael, Z. Kun, S. Zhi-xun, L. Xinxin, Journal of Micromechanics and Microengineering 2012, 22, 115040.
[30] K. Lai, W. Kundhikanjana, M. Kelly, Z. X. Shen, Review of Scientific Instruments 2008, 79, 063703.
[31] J. Seidel, L. W. Martin, Q. He, Q. Zhan, Y. H. Chu, A. Rother, M. E. Hawkridge, P. Maksymovych, P. Yu, M. Gajek, N. Balke, S. V. Kalinin, S. Gemming, F. Wang, G. Catalan, J. F. Scott, N. A. Spaldin, J. Orenstein, R. Ramesh, Nat Mater 2009, 8, 229.
[32] A. Tselev, P. Yu, Y. Cao, L. R. Dedon, L. W. Martin, S. V. Kalinin, P. Maksymovych, Nature Communications 2016, 7, 11630.
[33] E. Y. Ma, Y.-T. Cui, K. Ueda, S. Tang, K. Chen, N. Tamura, P. M. Wu, J. Fujioka, Y. Tokura, Z.-X. Shen, Science 2015, 350, 538.
[34] E. Y. Ma, B. Bryant, Y. Tokunaga, G. Aeppli, Y. Tokura, Z.-X. Shen, Nature Communications 2015, 6, 7595.
[35] A. Ying, B. Osting, I. C. Noyan, C. E. Murray, M. Holt, J. Maser, Journal of Applied Crystallography 2010, 43, 587.
[36] M. H. Holt, Ross; Winarski, Robert; Rose, Volker, Annual Review of Materials Research 2013, 43, 183.
[37] J. C. Baumert, P. Günter, H. Melchior, Optics Communications 1983, 48, 215.
[38] I. Biaggio, P. Kerkoc, L. S. Wu, P. Günter, B. Zysset, J. Opt. Soc. Am. B 1992, 9, 507.
[39] M. Zgonik, R. Schlesser, I. Biaggio, E. Voit, J. Tscherry, P. Günter, Journal of Applied Physics 1993, 74, 1287.
[40] R. C. Miller, Applied Physics Letters 1964, 5, 17.
[41] I. Shoji, T. Kondo, A. Kitamoto, M. Shirane, R. Ito, J. Opt. Soc. Am. B 1997, 14, 2268.

Supplementary References

[42] W. N. Herman, L. M. Hayden, J. Opt. Soc. Am. B 1995, 12, 416.
[43] B. Zysset, I. Biaggio, P. Günter, J. Opt. Soc. Am. B 1992, 9, 380.

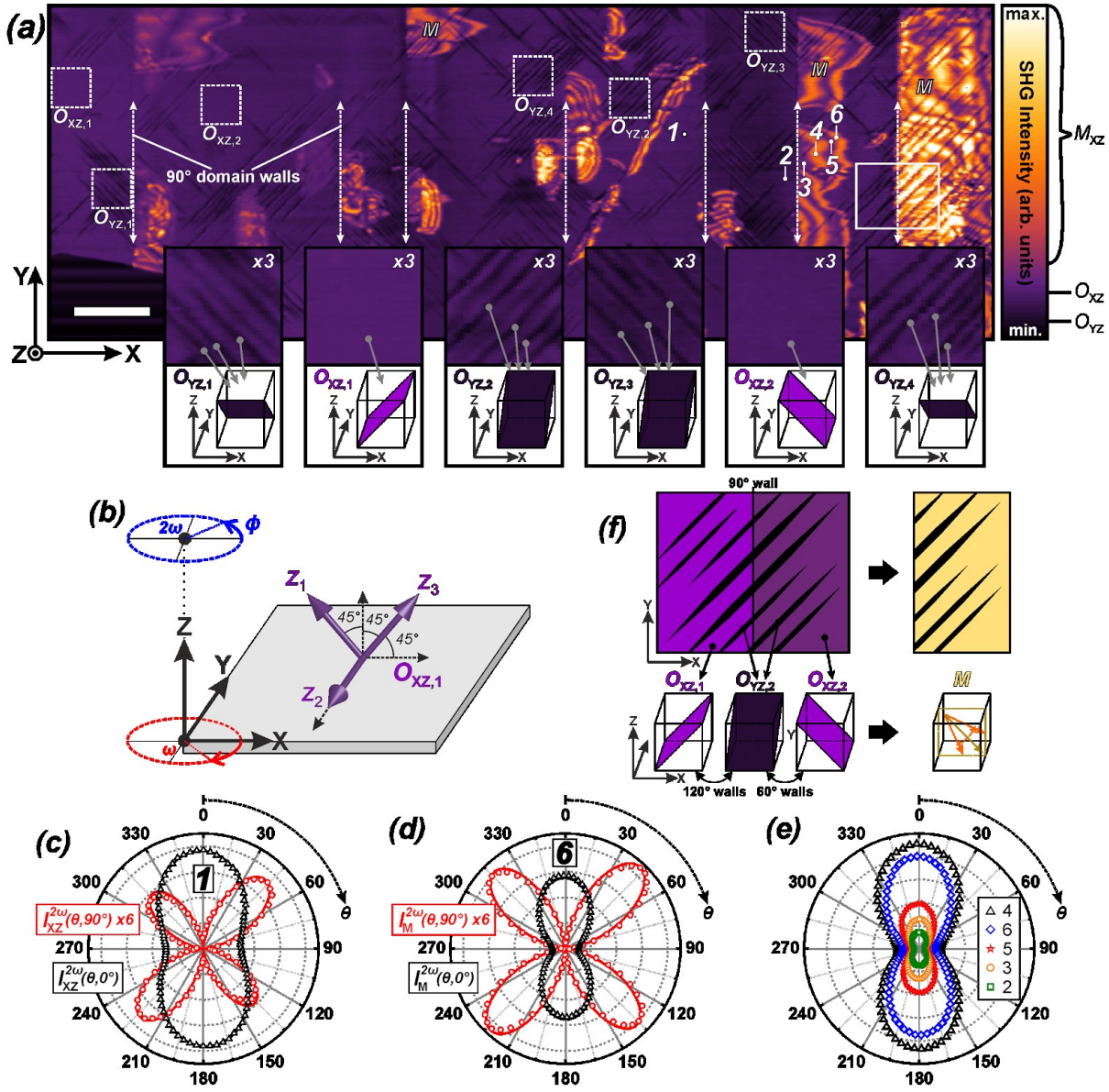

Figure 1. (a) Scanning SHG microscopy image ($I^{2\omega}(\theta, 0°)$) of a densely twinned domain structure in a $KNbO_3$ single crystal (surface ∥ $(001)_{pc}$). The image is composed of several stitched area scans (10% overlap). Scale bar: 50 µm. The proposed P_S directions in the various domains are depicted in the zoom-in insets (see text). The zero-signal area on the bottom left corresponds to a thin Ag marker pad that serves as a positional reference (see Experimental Section). (b) 3D sketch of the experimental geometry, indicating the XYZ reference coordinate system, the fundamental (θ) and SH (φ) polarization angles, and the crystal physics axes of the $O_{XZ,1}$ domain. (c) SHG intensity polar plots of $I_{XZ}^{2\omega}(\theta, 0°)$ and $I_{XZ}^{2\omega}(\theta, 90°)$ components (radius) versus the polarization angle (θ) of the fundamental light, measured on

position 1. Solid lines correspond to Equation S5 (*mm2* point group). Experimental data points in all polar plots are downsampled by a factor of two for clarity. (d) SHG intensity polar plots of $I_M^{2\omega}(\theta, 0°)$ and $I_M^{2\omega}(\theta, 90°)$ versus θ, measured on position 6. Solid lines correspond to Equation S8 (m point group). (e) Series of $I^{2\omega}(\theta, 0°)$ polar plots measured on positions 2 through 6 under the same experimental conditions. (f) Schematic depiction of O_{YZ} domains crossing a 90° O_{XZ} boundary, thereby necessarily forming charged and mechanically incompatible 60° domain walls on one side of that boundary, resulting in localized structural distortions that enable polarization rotation.

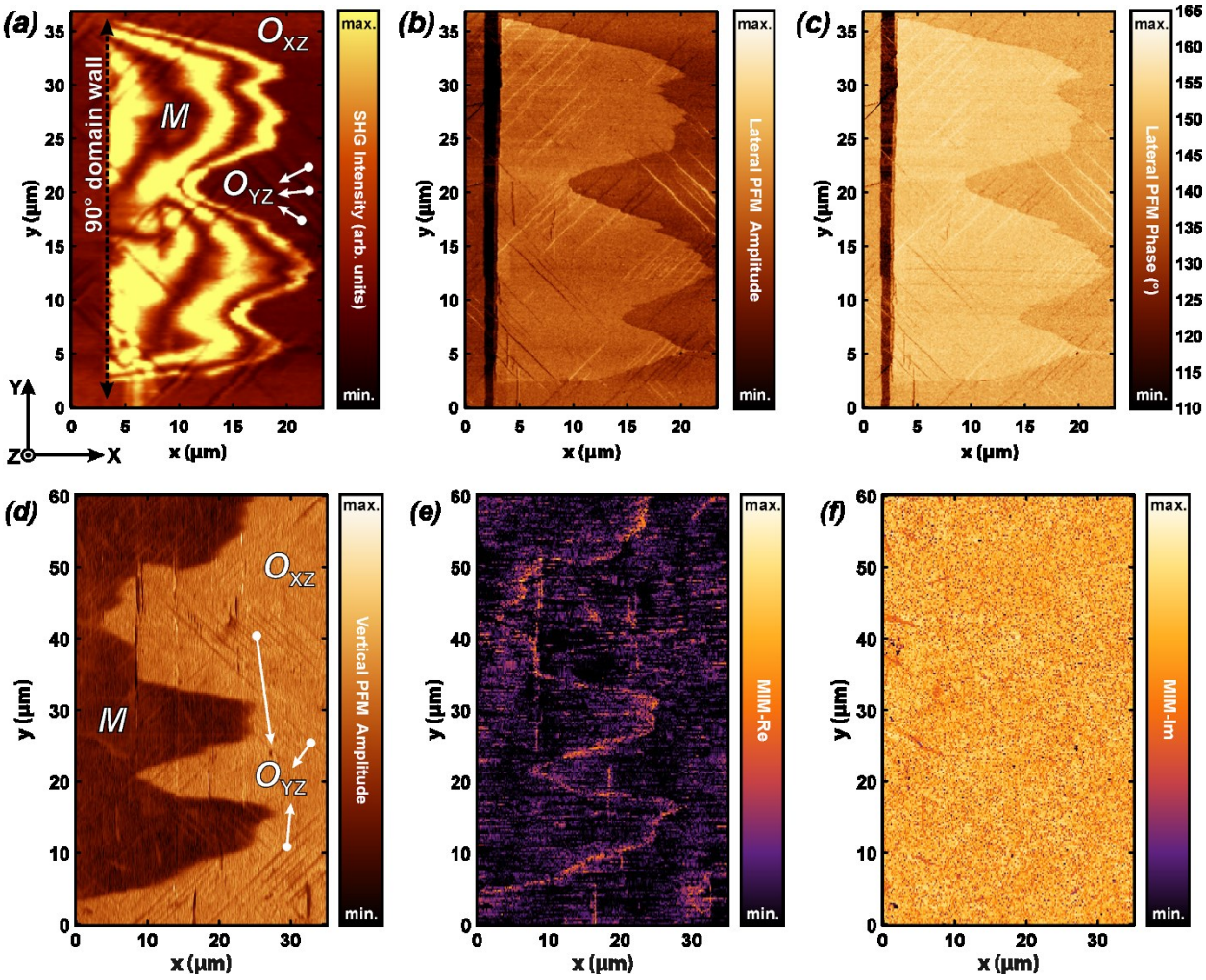

Figure 2. (a) Scanning SHG microscopy image ($I^{2\omega}(\theta, 0°)$) of a densely twinned domain structure in a $KNbO_3$ single crystal (surface ∥ $(001)_{pc}$). (b) Scanning PFM images of the same area recorded at CNMS (cantilever axis along x), showing: (b) lateral signal amplitude and (c) lateral signal phase contrast. (d) Scanning PFM image of a similar area on the same sample (recorded at UT Austin), plotting the vertical PFM amplitude. (e) Scanning MIM-Re and (f) MIM-Im images in the same area.

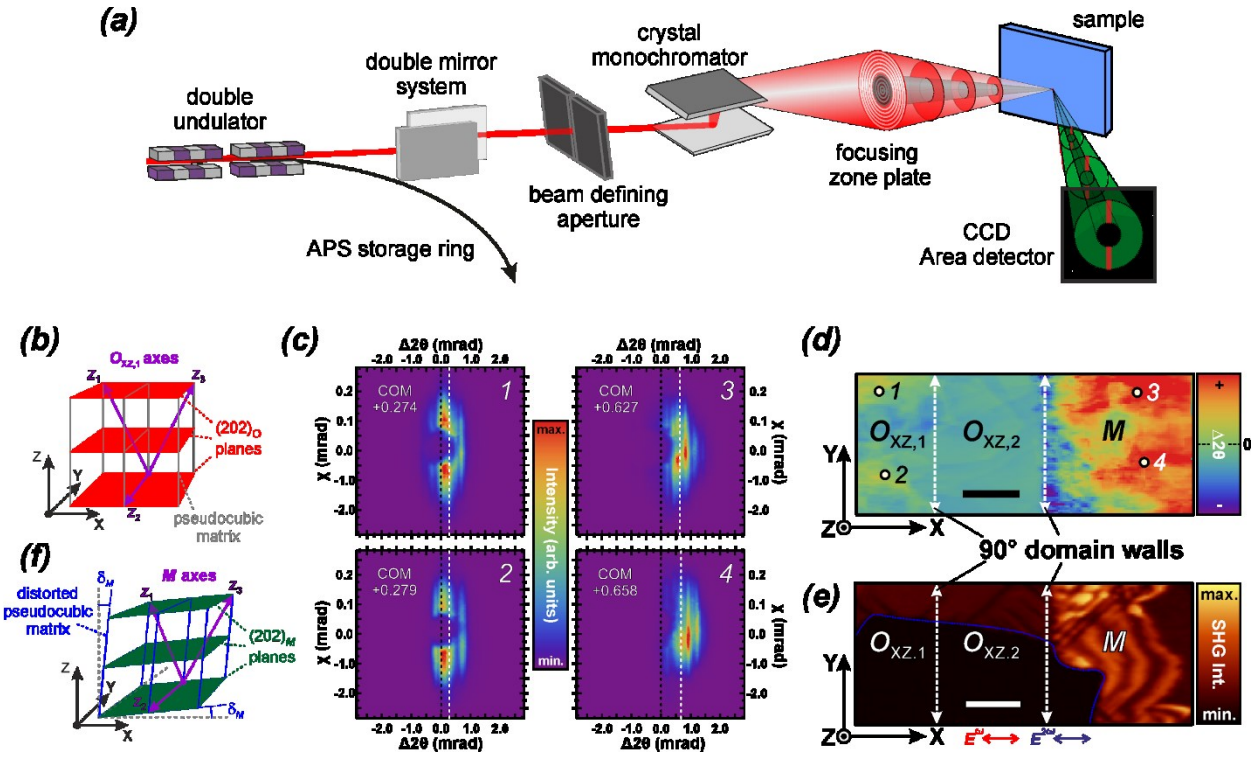

Figure 3. (a) Schematic of the SXDM setup. In this example the sample diffracts only the on-axis portion of the incident beam, corresponding to the center diffraction condition. (b) Sketch of the orthorhombic $O_{XZ,1}$ unit cell axes with respect to the pseudocubic matrix. The SXDM experiments were set up to probe the $(202)_O$ diffraction peak of the $O_{XZ,1}$ domains (shaded red planes). (c) Selected $O_{XZ,1}$ diffraction multiplets recorded in different positions. Black dashed lines indicate $\Delta 2\theta = 0$, white dashed lines indicate the relative 2θ-center-of-mass (COM) value of the shown multiplet. For reference, $\Delta 2\theta = 0$ refers to $2\theta = 36.7323°$, which corresponds to the 2θ-COM value of an untwinned orthorhombic $O_{XZ,1}$ domain. (d) Scanning SXDM image of a densely twinned area in the $KNbO_3$ sample, plotting the relative 2θ-COM value of the recorded $(202)_O$ diffraction of the $O_{XZ,1}$ domains. Numbers label the positions corresponding to the diffraction multiplets in panel c. Scale bar: 5 µm. (e) Scanning SHG microscopy image ($I^{2\omega}(\theta, 0°)$) of the same area. The zero signal area bordered by the blue dashed line corresponds to a thin silver pad that serves as a positional marker (see Experimental Section). Scale bar: 5 µm. (f) Sketch of the proposed simple shear deformation of the pseudocubic matrix, which tilts

the $(202)_M$ planes and the corresponding diffraction multiplets. The distortion results in a local monoclinic *m* symmetry, with the surviving mirror plane parallel to the XZ plane.

Supporting Information

Emergent Low-Symmetry Phases with Large Property Enhancement in Ferroelectric $KNbO_3$ Bulk Crystals

By *Tom T. A. Lummen, J. Leung, Amit Kumar, X. Wu, Y. Ren, Brian K. Vanleeuwen, Ryan C. Haislmaier, Martin Holt, Keji Lai, Sergei V. Kalinin, Venkatraman Gopalan**

1. Optical SHG Modeling for the Orthorhombic and Monoclinic $KNbO_3$ Phases.

We first consider the experimental geometry sketched in Figure 1b of the main text. The fundamental beam of frequency ω propagates in the -Z direction of reference coordinate system XYZ, with the azimuthal angle θ indicating the in-plane polarization of the corresponding electric field, $\mathbf{E}^{\omega}(\theta)$. After nonlinear interaction with the $KNbO_3$ crystal, the reflected second harmonic (SH) light (at frequency 2ω) is detected at a polarization given by angle φ. The corresponding general form of the reflected SHG intensity from a birefringent material at normal incidence can be derived as:[23, 42]

$$I^{2\omega}(\theta,\phi) = \frac{C}{\left(1+n^{\omega}(\theta)\right)^2\left(1+n^{2\omega}(\theta)\right)^2\left(n^{\omega}(\theta)+n^{2\omega}(\theta)\right)^2}\left[\sum_i P_i^{2\omega}(\theta)A_i^{2\omega}(\phi)\right]^2, \quad \text{(S1)}$$

$$\text{with } P_i^{2\omega}(\theta) = \sum_{j,k} d_{i,j,k}E_j^{\omega}(\theta)E_k^{\omega}(\phi) \quad \text{(S2)}$$

where C is a constant of proportionality (containing among others the square of the incident light intensity and the detector efficiency), $n^{\omega}(\theta)$ and $n^{2\omega}(\theta)$ are the refractive indices of the material for fundamental and SH light polarized at angle θ, $\boldsymbol{P}^{2\omega}$ is the induced second harmonic polarization, $\boldsymbol{A}^{2\omega}$ is the vector corresponding to the SH polarization analyzer, and d is the third-rank nonlinear optical tensor of the material. The appropriate birefringence at both ω and 2ω was calculated using the corresponding Sellmeier equations for $KNbO_3$ determined

by Zysset *et al*.[43] From here on, we will make use of the inherent symmetry of the nonlinear optical tensor ($d_{ijk} = d_{ikj}$) and express its elements in the contracted Voigt form d_{ij}, where *i* = 1,2,3 and *j* = 1,2,3,4,5,6 refer to the standard crystal physics axes adopted for the appropriate point group.[22]

For orthorhombic $KNbO_3$ (point group *mm2*) in the above geometry, the SHG response from each of the four symmetry-equivalent XZ domains (polarization along one of the $\langle 101 \rangle_{pc}$ axes) is exactly the same, such that we need consider only one such case. The general nonlinear optical tensor of the *mm2* point group, expressed in terms of the standard crystal physics axes z_1, z_2 and z_3 is:[22]

$$d^{mm2} = \begin{pmatrix} 0 & 0 & 0 & 0 & d_{15} & 0 \\ 0 & 0 & 0 & d_{24} & 0 & 0 \\ d_{31} & d_{32} & d_{33} & 0 & 0 & 0 \end{pmatrix}. \tag{S3}$$

As it is convenient to work in the experimental reference frame, we next use an axes transformation to express this tensor in the XYZ coordinate system. For the sake of consistency we again choose the case of the $O_{XZ,1}$ domains, for which the crystal physics axes are such that the polar z_3 axis lies along the [101] direction, z_2 lies along the [0-10] direction, and z_1 lies along the [-101] direction (see sketch in Figure 1b). The corresponding transformed nonlinear optical tensor becomes:

$$d_{XZ}^{mm2} = \begin{pmatrix} \frac{d_{15}+d_{31}+d_{33}}{2\sqrt{2}} & \frac{d_{32}}{\sqrt{2}} & \frac{-d_{15}+d_{31}+d_{33}}{2\sqrt{2}} & 0 & \frac{-d_{31}+d_{33}}{\sqrt{2}} & 0 \\ 0 & 0 & 0 & \frac{d_{24}}{\sqrt{2}} & 0 & \frac{d_{24}}{\sqrt{2}} \\ \frac{-d_{15}+d_{31}+d_{33}}{2\sqrt{2}} & \frac{d_{32}}{\sqrt{2}} & \frac{d_{15}+d_{31}+d_{33}}{2\sqrt{2}} & 0 & \frac{-d_{31}+d_{33}}{\sqrt{2}} & 0 \end{pmatrix}. \tag{S4}$$

After correction for the measured experimental offset in the polarization of the fundamental light ($\Delta\theta$ = -1.9 ± 0.2°), we obtain the following expressions for the reflected SHG intensity:

$$I_{XZ}^{2\omega}(\theta, 0°) \propto \tfrac{1}{8}\left[\cos(\Delta\phi)\left(\alpha\cos^2(\theta) + \beta\sin^2(\theta)\right) + \gamma\sin(\Delta\phi)\sin(2\theta)\right]^2 \approx \tfrac{1}{8}\left[\alpha\cos^2(\theta) + \beta\sin^2(\theta)\right]^2 \tag{S5a}$$

$$I_{XZ}^{2\omega}(\theta, 90°) \propto \tfrac{1}{8}\left[\sin(\Delta\phi)\left(\alpha\cos^2(\theta) + \beta\sin^2(\theta)\right) - \gamma\cos(\Delta\phi)\sin(2\theta)\right]^2 \approx \tfrac{1}{8}\left[\gamma\sin(2\theta)\right]^2 \tag{S5b}$$

$$\text{with } \alpha = d_{15} + d_{31} + d_{33},\ \beta = 2d_{32}, \text{ and } \gamma = -2d_{24} \tag{S5c}$$

where $\Delta\varphi$ = -1.6 ± 0.1° is the experimental offset in the polarization of the detected SH light. Equations 5 are simultaneously fit to both complementary SHG polarimetry data sets measured in an $O_{XZ,1}$ domain (position 1 in Fig. 1a), using α, β and γ as fit parameters. The resulting relative parameter values are summarized in **Table S1**.

Table S1. Fit parameters and standard errors of the orthorhombic (*mm*2) and monoclinic (*m*) SHG polarimetry models.

	Position 1 (*mm*2, Equation 5)	Position 6 (*m*, Equation 8)
β^m / α^m	0.729±0.001	0.490±0.002
γ^m / α^m	0.41±0.02	0.54±0.08

Next we consider the symmetry in the *M* domains of strongly enhanced SHG intensity (See Figure 1a). As was shown for $BaTiO_3$, the structural distortion associated with the thermotropic phase corresponds to a lowered local symmetry, which allows for the rotation of the ferroelectric polarization within one of the surviving mirror planes of the parent point group. In the case of the O_{XZ} domain matrix here, there are two orthorhombic mirror planes: one oriented parallel to the XZ plane, and another parallel to the Z_2Z_3 plane (see Figure 1b), of which one mirror is broken upon the rotation of the polarization in the other mirror plane. Although a model with either surviving mirror plane could in principle match the experimental polarimetry data (Figure 1d), we consider only the former case here explicitly, as the latter merely yields more complicated expressions of an identical functional form, with additional cross-terms and fit parameters. With the surviving mirror plane parallel to the XZ plane, the general nonlinear optical tensor of the monoclinic *m* point group, expressed in terms of the standard crystal physics axes z_1, z_2 and z_3 is:[22]

$$d^m = \begin{pmatrix} d_{11}^m & d_{12}^m & d_{13}^m & 0 & d_{15}^m & 0 \\ 0 & 0 & 0 & d_{24}^m & 0 & d_{26}^m \\ d_{31}^m & d_{32}^m & d_{33}^m & 0 & d_{35}^m & 0 \end{pmatrix}. \quad \text{(S6)}$$

We again transform this tensor to the experimental XYZ reference frame, keeping the crystal physics axes as defined before (Figure 1b), yielding:

$$d_M^m = \begin{pmatrix} \frac{-d_{11}^m - d_{13}^m + d_{15}^m + d_{31}^m + d_{33}^m - d_{35}^m}{2\sqrt{2}} & \frac{-d_{12}^m + d_{32}^m}{\sqrt{2}} & \frac{-d_{11}^m - d_{13}^m - d_{15}^m + d_{31}^m + d_{33}^m + d_{35}^m}{2\sqrt{2}} & 0 & \frac{d_{11}^m - d_{13}^m - d_{31}^m + d_{33}^m}{\sqrt{2}} & 0 \\ 0 & 0 & 0 & \frac{d_{24}^m + d_{26}^m}{\sqrt{2}} & 0 & \frac{d_{24}^m - d_{26}^m}{\sqrt{2}} \\ \frac{d_{11}^m + d_{13}^m - d_{15}^m + d_{31}^m + d_{33}^m - d_{35}^m}{2\sqrt{2}} & \frac{d_{12}^m + d_{32}^m}{\sqrt{2}} & \frac{d_{11}^m + d_{13}^m + d_{15}^m + d_{31}^m + d_{33}^m + d_{35}^m}{2\sqrt{2}} & 0 & \frac{-d_{11}^m + d_{13}^m - d_{31}^m + d_{33}^m}{\sqrt{2}} & 0 \end{pmatrix}, \quad \text{(S7)}$$

and obtain the following expressions for the reflected SHG intensity ($\Delta\theta$ = -1.3 ± 0.2°):

$$I_M^{2\omega}(\theta, 0°) \propto \tfrac{1}{8}\left[\cos(\Delta\phi)\left(\alpha^m \cos^2(\theta) + \beta^m \sin^2(\theta)\right) + \gamma^m \sin(\Delta\phi)\sin(2\theta)\right]^2 \approx \tfrac{1}{8}\left[\alpha^m \cos^2(\theta) + \beta^m \sin^2(\theta)\right]^2 \quad \text{(S8a)}$$

$$I_M^{2\omega}(\theta, 90°) \propto \tfrac{1}{8}\left[\sin(\Delta\phi)\left(\alpha^m \cos^2(\theta) + \beta^m \sin^2(\theta)\right) - \gamma^m \cos(\Delta\phi)\sin(2\theta)\right]^2 \approx \tfrac{1}{8}\left[\gamma^m \sin(2\theta)\right]^2 \quad \text{(S8b)}$$

$$\text{with } \alpha^m = d_{11}^m + d_{13}^m - d_{15}^m - d_{31}^m - d_{33}^m + d_{35}^m, \beta^m = 2(d_{12}^m - d_{32}^m), \text{ and } \gamma^m = 2(d_{24}^m - d_{26}^m) \quad \text{(S8c)}$$

where $\Delta\varphi$ = -0.7 ± 0.1°. These intensity expressions have the same functional form as those found for the orthorhombic XZ domains (Equation 5), but with different parameters in terms of the linear combinations of the nonlinear optical tensor elements. Moreover, as these elements corresponds different phases, the monoclinic d_{ij}^m can strongly differ from the orthorhombic d_{ij} in both magnitude and sign. Equation 8 simultaneously fits to both complementary polarimetry data sets measured in an *M* domain; the resulting relative fit parameters α^m, β^m, and γ^m are given in **Table S1**.

Comparing the SHG polarimetry data taken in the O_{XZ} and *M* domains (positions 1 and 6 in Figure 1), the $I^{2\omega}(\theta, 0°)$ data from the *M* domain exhibit signal intensity nodes that are more pinched (at θ = 90 and 270°), which is reflected in the significantly lower relative contribution of the β^m coefficient. In addition, the intensity ratio between $I^{2\omega}(\theta, 90°)$ and $I^{2\omega}(\theta, 0°)$ is larger in the *M* domain, resulting in a larger relative value of γ^m as compared to γ. Although the orthorhombic model has the same functional form as the monoclinic model, it cannot account for the large local SHG intensity enhancements observed in the *M* domains,

because its intensity is restricted by the nominal nonlinear optical tensor coefficients of orthorhombic $KNbO_3$ (the d_{ij} values).

2. Out-of-plane PFM response

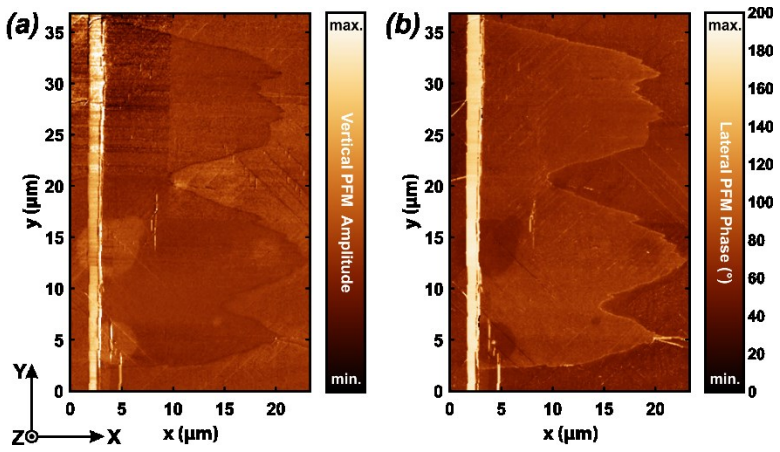

Figure S1. Scanning PFM images of the same area of the $KNbO_3$ domain microstructure as shown in Figure 2a through 2c. Panels show the (a) PFM vertical signal amplitude and (b) vertical signal phase, respectively, which nominally contain the combined contributions of the d_{31}, d_{33}, and d_{15} piezoelectric coefficients. Data was recorded at CNMS, with the cantilever axis along the x axis.

3. Finite Element Analysis of the MIM response

The MIM-Re and MIM-Im signals are proportional to the real and imaginary parts of the tip-sample admittance, which can be computed by the software COMSOL 4.4. Since the DW width w is much smaller than the tip diameter d, the simulation result is invariant with respect to the DW sheet conductance $s_{DW} \times w$, as shown in **Figure S2**. Here $d = 200$ nm and $w = 2$ nm are used in the modeling. Although the signal-to-noise ratio is low in our data, the DW contrast (with respect to the insulating domains) is clearly discernible in the MIM-Re channel and below the noise floor in the MIM-Im channel, if any. The comparison between the FEA simulation and our experimental data indicates that the DW exhibits a sheet conductance

around $10^{-8} \sim 10^{-9}$ W^{-1}. In other words, the local conductivity of DWs separating the M domains and the O_{XZ} domains is about 1 S m^{-1}, similar to that of other ferroelectric DWs such as $BiFeO_3$ and PZT.[31, 32]

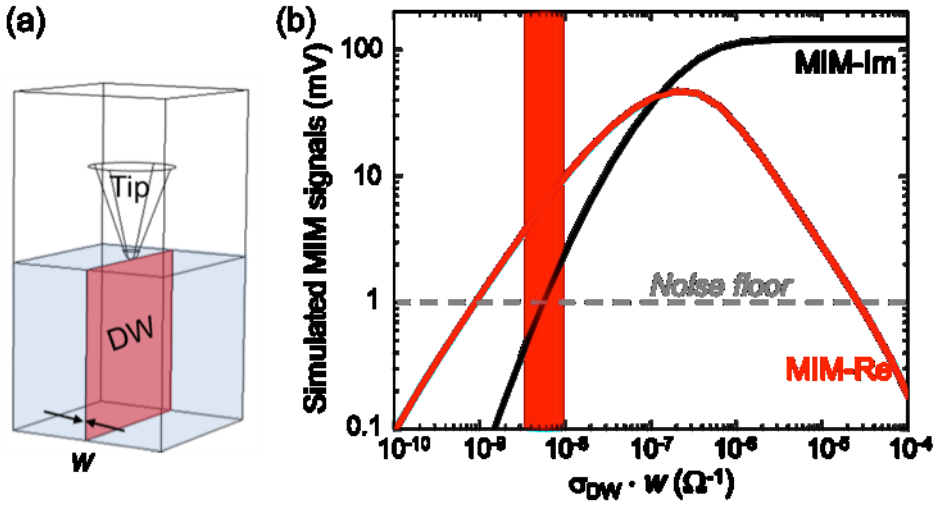

Figure S2. (a) 3D modeling geometry of the FEA simulation. The DW is modeled as a sheet of conductor with a width of *w* and conductivity of s_{DW}. (b) Simulated MIM signals as a function of the sheet conductance $s_{DW} \times w$ of the DW. The measured DW contrast is highlighted in red, indicating the discernible MIM-Re and negligibly small (below noise floor) MIM-Im signals.

Supplementary References

[42] W. N. Herman, L. M. Hayden, J. Opt. Soc. Am. B 1995, 12, 416.
[43] B. Zysset, I. Biaggio, P. Günter, J. Opt. Soc. Am. B 1992, 9, 380.